JTTEE5 12:377-392
© ASM International

Influence of Process Parameters on the Deposition Footprint in Plasma-Spray Coating

K. Remesh, H.W. Ng, and S.C.M. Yu

(Submitted 11 December 2001; in revised form 25 October 2002)

This paper presents an investigation of the influence of plasma spray process conditions on the in-flight particle behavior and their cumulative deposition to form a coating on the substrate. Three-dimensional computational fluid dynamics (CFD) analyses were performed to model the in-flight particle behavior in the plasma-spray process and their deposition on the substrate. The plasma spray was modeled as a jet issuing from the torch nozzle through the electrical heating of the arc gas. In the model, particles were injected into the plasma jet where they acquired heat and momentum from the plasma, some got melted and droplets were formed. By means of a droplet splatting model, the particle in-flight data generated by the CFD analyses were further processed to build up an imaginary three-dimensional deposition profile on a flat stationary substrate. It is found that the powder carrier gas flow rate influences the particle distribution on the substrate by imparting an injection momentum to the particles that were directed radially into the plasma jet in a direction perpendicular to the plasma jet. The larger sized particles will acquire higher injection momentum compared with the smaller sized particles. This causes particle distribution at the substrate surface that is elliptical in shape with the major axis of ellipse parallel to the particle injection port axis as illustrated in Fig. 1. Larger particles tend to congregate at the lower part of the ellipse, due to their greater momentum. The distribution of particle size, temperature, velocity, and count distribution at the substrate was analyzed. Further, based on the size and the computed particle temperature, velocity histories, and the impact sites on the substrate, the data were processed to build up a deposition profile with the Pasandideh-Fard[1] model. The shapes of deposition profiles were found to be strongly driven by the segregation effect.

Keywords coating deposition, computational modeling, plasma spray, splat model

1. Introduction

Thermal spray is a coating process used to produce protective coatings for a wide range of applications. The thermal spray deposit parameters such as thickness, porosity, and efficiency of deposition are dependent on the process parameters, powder feedstock, and hardware configuration. The controllable process parameters such as torch power, arc gas flow rate, and carrier gas flow rate influence the plasma velocity and temperature characteristics. These in turn control particle velocity, temperature, and size on depositing on the substrate. The ability of plasma-sprayed coating to sustain service stress is closely correlated to the microstructure.[2,3] Improving the understanding of the relationship between microstructure as well as deposited profile of thermally sprayed coating to the spray parameters would require a predictive capability.

A physically based computational fluids dynamics (CFD) process allows for the prediction of the particle temperature, velocity, and size distributions, which indirectly are used to derive the deposit, profiles on the substrate. This paper shows that particle segregation or classification based upon size occuring in the plasma plume is due to the momentum effects. The smallest-sized particles having lowest momentum are unable to penetrate the plasma plume and tend to populate near the injector side. However, the largest of the particles with greatest momentum went further and ended on the opposite side of the plume. The experimental work by Cetegen and Yu[4] and other researchers[5-11] have shown that aerodynamic classification of particles causes the larger particles to concentrate on the lower part of the plasma jet. This effect is graphically illustrated in Fig. 1.

The particle temperature, velocity, and size at various impact locations of the substrate can vary widely. The study by Kucuk et al.[11] have shown that particle temperature and velocity in the same plume vary by 400 °C and 100 m/s, respectively, depending on location. As the substrate is bombarded with particles of different sizes, velocities, and temperatures at different locations simultaneously, it is inevitable that significant nonuniformity in the coating thickness and microstructure will result.

This paper is an extension of an earlier paper,[12] which reported on the spatial distribution of particle parameters such as temperature, velocity, and size in the plasma plume and their comparison with experimental measurements. In the paper, the authors compared their simulation predictions with a well-documented experimental measurement of in-flight particle temperatures, size, and velocities published by Kucuk et al.[11] The simulations were performed for the same operating conditions as the in-flight experiments were conducted. Communication between the first author and Kucuk at the State University of New York at Stony Brook was initiated to establish the modeling details. A fairly close agreement obtained between the predictions and experimental results offered a fair degree of confidence on the validity of the simulation. The earlier paper also investigated in detail the location of particle impact on the sub-

---

K. Remesh, H.W. Ng, and **S.C.M. Yu,** School of Mechanical & Production Engineering, Nanyang Technological University, Nanyang Avenue, Singapore 639798. Contact e-mail: mhwng@ntu.edu.sg.

strate and concentration of particles relating to their size and location on the substrate. Using the simulation output, it is possible to simulate the splat formation and spread, deposit build up, and hence investigate the influence of process parameters on deposit topology. The methodology of generating the deposit topology by simulation and results obtained are now presented in the current paper.

The paper first describes the computational calculations utilizing the FLUENT V5.4 (Centerra Resources Park, Lebanon, NH) software that provides output data such as particle in-flight temperatures, velocities, sizes, and sites of impact at the substrate. After discounting the particles that remain solid (having a temperature below melting point), the remaining melted droplets will splat on the substrate. Various splatting models, based on either analytical[1,13-16] or empirical[17,18] approach, have been proposed. It is noted that the predictions of these models often differ widely; however, most agree that the factors of surface roughness, temperature, particle velocity, temperature, sizes, viscosity, surface tension, and angle of impact governed the splat spread. Furthermore, substrate geometry, liquid-solid contact angle between the droplet and substrate, heat transfer between the droplet and substrate, and surface thermal properties further complicated the issue.[1] Thus, due to the many uncertainties and lack of physical properties data required to use the model, they should be used with caution. The use of such models to build up a deposit yields a qualitative picture of the deposit process. However, it has sufficient merit in taking account of the most important physical mechanisms at present to allow a comparison of how different plasma spray operational parameters would affect the deposit profile.

Nomenclature

A_p	particle surface area, m^2
c	species concentration, kg/m^3
C_D	drag coefficient, dimensionless
c_p	specific heat capacity, J/kgK
d	splat diameter, m
D_p	particle diameter, m
D_{ij}	binary diffusion coefficient, m^2/s
F_D	drag force experienced by particle, N
h	heat transfer coefficient, W/m^{2}K
H_{sf}	latent heat of melting, J/kg
K	turbulent kinetic energy per unit mass, m^2/s^2
k	thermal conductivity, W/mK
m_p	particle mass, kg
Nu	Nusselt number, dimensionless
P	pressure, Pa
P'''_{in}	volume averaged power source term, W/m^3
P_r	Prandtl number, dimensionless
Pe	Peclet number, dimensionless
Re	Particle Reynolds number, dimensionless
St	Stefan number, dimensionless
t	time, s
T	gas temperature, K
T_{bp}	particle boiling point, K
T_{mp}	particle melting point, K
T_p	particle temperature, K
u	axial velocity, m/s
u_p	particle axial velocity, m/s
V	plasma velocity, m/s
We	Weber number, dimensionless
x	mole fraction of species, dimensionless

Greek Symbols

α	thermal diffusivity, m^2/s
ε	dissipation rate of turbulent kinetic energy, m^2/s^3
μ	dynamic viscosity, kg/ms
ν	kinematic viscosity, m^2/s
ρ	fluid density, kg/m^3
σ	surface tension, N/m
ξ	spread factor, dimensionless
ζ	liquid fraction, dimensionless

Subscripts

l	laminar
o	initial
p	particle
t	turbulent

The Pasandideh-Fard model[1] was chosen for this study because it incorporates most of the contributing factors. A Fortran program was written to calculate the circular splats as flat disk diameter and thickness by the splatting model and lays the disks down on a flat plane, locating the disk centers at the impact sites of the particles. The program read all the particle data, carried out calculations particle by particle, and accumulated the thickness build-up on a surface mesh, representing the substrate. The calculations produced three-dimensional deposits for stationary as well as traversing torch spraying on a stationary substrate. The various cases analyzed for different torch operating conditions will show the effect of the different operating parameters on the deposit topology.

The deposit efficiency is strongly linked to the number of particles that achieve the melting temperature and significant velocity. The amount of heat and kinetic energies of the injected particles on reaching the substrate are indications of deposit efficiency since the deposition depends on the degree of melting and impact velocity. To quantify the amount of heat and kinetic energy acquired by the injected particles, mass averaged particle temperature and velocity were calculated and analyzed for the effect of process parameters on the above quantities. The first part of the paper evaluated statistically useful parameters based upon temperature and velocity to enable quick checks on the efficiency of the process followed by the splat deposition profile.

2. Problem Definition and Modeling

As shown in the schematic diagram in Fig.1, the main plasma spray components consist of a plasma torch and a powder injection port, in this case delivering powder external to the torch. A high-temperature and -velocity plasma jet is created and maintained by a direct current arc in the torch, which ejects to the atmosphere. Powder was fed by first mixing with a carrier gas in a powder hopper and injected into the plasma jet radially through the external injection port. The powder henceforth will be referred to as particles. The particles are propelled and heated by the plasma jet and if melted are deposited on the substrate, which

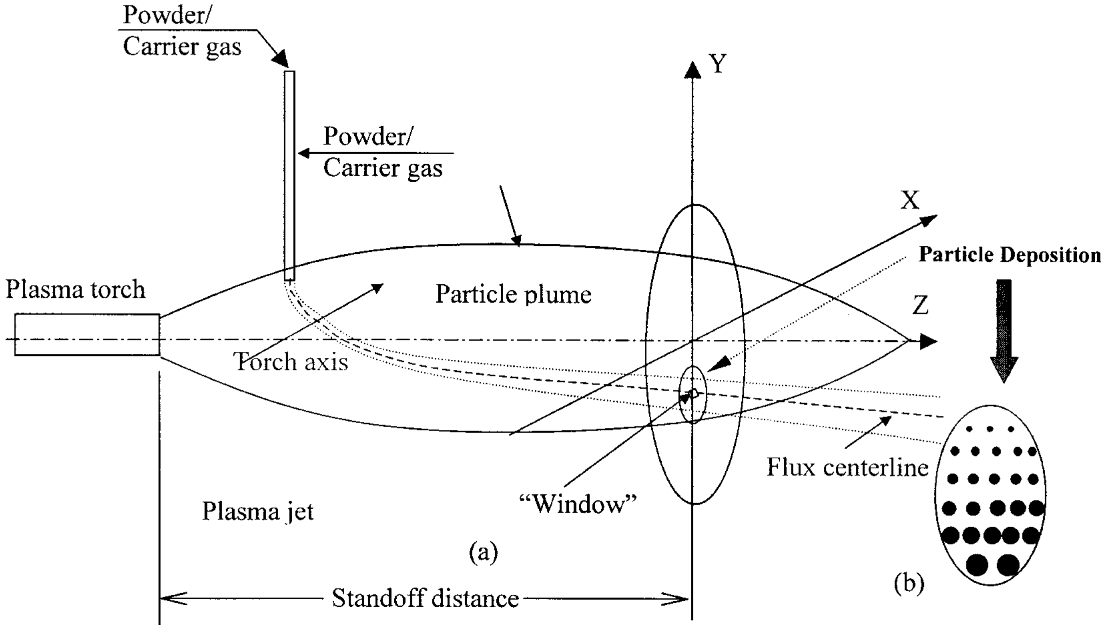

Fig. 1 **(a)** Schematic diagram of plasma spray process with the particle plume cross section, and **(b)** particle segregation at the substrate

is usually positioned at the standoff distance, typically 80-100 mm.

The detailed mathematical model and solution procedure is presented in Ref. 12. For completeness, a summarized description of the process is given below. The arc gases are mixed Ar-H_2, the carrier gas is pure N_2, and the powder is yttria partially stabilized zirconia (METCO 204 NS), (Sulzer Metco Inc., Westbury, NY).

2.1 Governing Equations

The governing equation for plasma flow is shown below:

$$\nabla \cdot (\rho V\phi) = \nabla \cdot (\Gamma_\phi \nabla\phi) + S_\phi \qquad \text{(Eq 1)}$$

with ϕ as the process variable. The diffusion coefficients Γ_ϕ for the different conservation equations are given in Table 1 and all other notations are provided in the nomenclature. The solution of Eq 1 together with the associated boundary conditions gives the spatial distributions of plasma gas temperature, velocities, and pressures.

The particle dynamics and energy equations, which govern the velocity and trajectory of each particle within the jet, are shown below:

$$m_\mathrm{p}\frac{\mathrm{d}u_\mathrm{p}}{\mathrm{d}t} = F_\mathrm{D} \qquad \text{(Eq 2)}$$

i.e.,

$$\frac{\mathrm{d}u_\mathrm{p}}{\mathrm{d}t} = \frac{l8\mu}{\rho_\mathrm{p} D_\mathrm{p}^2}\frac{C_\mathrm{D} Re}{24}(u - u_\mathrm{p}) \qquad \text{(Eq 3)}$$

Table 1 The Process Variables, Diffusion Coefficient, and Source Term for Governing Eq 1

Governing Equation	Variable, ϕ	Diffusion Coefficient, Γ_ϕ	Source Term, S_ϕ
Mass	l	…	…
Momentum	u, v, w	ν	…
Energy	T	α	P'''_in
Species	x_i	D_Ij	…
Turbulence	k, ϵ	γ_t	…

$$\text{where } Re = \frac{\rho D_\mathrm{p} u_\mathrm{p} - u}{\mu} \qquad \text{(Eq 4)}$$

$$\text{and } C_\mathrm{D} = a_1 + \frac{a_2}{Re} + \frac{a_3}{Re^2} \qquad \text{(Eq 5)}$$

The governing equations for the heat transfer to the particles for determination of the particle temperature are shown below:

$$hA_\mathrm{p}(T_\infty - T_\mathrm{p}) = m_\mathrm{p} c_\mathrm{p}\frac{\mathrm{d}T_\mathrm{p}}{\mathrm{d}t} + m_\mathrm{p} H_\mathrm{sf}\frac{\mathrm{d}\zeta}{\mathrm{d}t} \qquad \text{(Eq 6)}$$

where ζ is the liquid fraction that takes into account the latent heat of fusion required to melt the particle.

The heat transfer coefficient h was evaluated using the Ranz and Marshall correlation:

$$N_\mathrm{u} = \frac{hD_\mathrm{p}}{k} = 2.0 + 0.6\, Re^{1/2}\, Pr^{1/3} \qquad \text{(Eq 7)}$$

The particle heating model in Eq 6 assumes that each particle will have a uniform temperature, neglecting the radial temperature gradient inside the particle. Based on this model, heat trans-

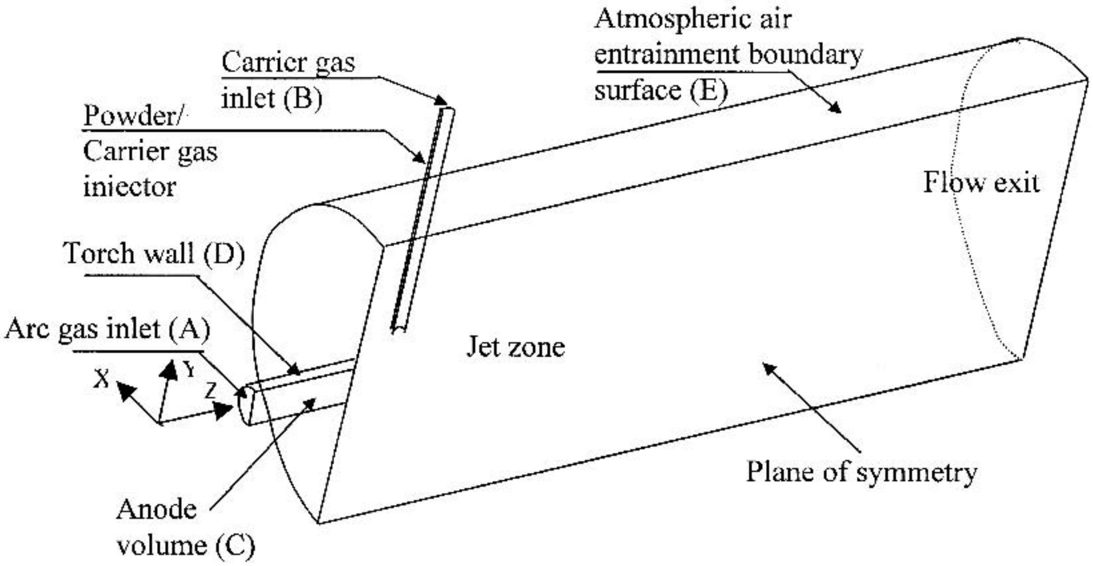

Fig. 2 Schematic diagram of plasma spray process with computational domain that consisted of anode, particle/carrier gas injector, and the jet zone

fer from plasma to particle is by convection; heat gained raises the solid particle temperature with the liquid fraction ζ initially zero. As the particle temperature reaches the melting point, a solid to liquid phase change occurs at the surface of the particles; heat transfer then supplies heat energy for latent heat of fusion. As the liquid fraction ζ approaches 1.0, the particles gradually become fully liquid, i.e., molten, during which the particle temperature remains constant at the melting point. When melting is completed, ζ =1.0, the particle temperature will start to rise again with continuing heat absorption.

The governing equations were solved using FLUENT for the three-dimensional domain as depicted in Fig. 2. The computational domain consisted of the anode (*D*), the jet zone and the powder/carrier gas port. The size of anode was ϕ7.8 × 18.5 mm, the jet zone was ϕ70 × 220 mm, and the carrier gas port was ϕ2.2 × 50 mm. The injector port was located at 7 mm away from the nozzle exit and 9 mm above the nozzle axis. The governing equations were solved using a grid having 14 × 24 × 27 cells for nozzle region, 70 × 24 × 120 cells in the free jet region, and 8 × 18 × 63 cells at the powder/ carrier gas injector.

Computations were carried out for process cases set out in Table 2. The cases S1 to S6 refer to those operational settings of the plasma spray used in the experimental in-flight measurements by Kucuk et al.[11,19] Cases S1 to S4 were performed to study the effect of carrier gas flow rate on the deposit topology. Cases S4 and S5 enabled the effect of arc gas flow rates to be studied while cases S5 and S6 isolated the effect of torch power input. The substrate is imagined to be stationary at a standoff distance of 80 mm for all cases.

2.1.1 Properties of Gases and Powder. The temperature dependent gas transport properties for Ar, H_2, and N_2 such as density, viscosity, specific heat, and thermal conductivity are based upon the work of Boulose et al.[20] To allow for the determination of the values of the properties at the cell temperature during the iteration, property values were incorporated in the FLUENT model as piece-wise linear profiles with respect to temperature.

Table 2 Spray Parameters for Numerical Prediction of Particle Performance

Cases	S1	S2	S3	S4	S5	S6
Torch power input, kW	42	42	42	42	42	33
Primary gas (Ar) flow rate, slm	40	40	40	40	50	50
Secondary gas (H_2) flow rate, slm	12	12	12	12	11	11
Ratio of primary to secondary gas flow rate	3.3	3.3	3.3	3.3	4.54	4.54
Carrier gas (N_2) flow rate, slm	2.0	4.0	6.0	3.5	3.5	3.5

Mixing rules were used to determine the properties of the mixture that constitutes the arc gas, the carrier gas, and the atmospheric air. The density of the mixture of the multicomponent gas mixtures was calculated using the mass averaged equation as follows:

$$\rho = \frac{1}{\sum_i \frac{y_i}{\rho_i}} \quad \text{(Eq 8)}$$

where y_i is the mass fraction.

The viscosity of the mixture is computed based on a simple mass fraction average of the pure species viscosity:

$$\mu = \sum_i y_i \mu_i \quad \text{(Eq 9)}$$

The thermal conductivity of the mixture was computed based on a simple mass fraction average of the pure species conductivity:

$$k = \sum_{i} y_i k_i \qquad \text{(Eq 10)}$$

The specific heat capacity of the mixture was calculated as a mass fraction average of the pure species heat capacities:

$$c_p = \sum_{i} y_i c_{pi} \qquad \text{(Eq 11)}$$

The yttria-stabilized zirconia powder physical and thermal properties were obtained from Ref. 21 as shown in Table 3.

2.2 Data Analysis of FLUENT Output

The plane of the substrate was divided into number of cells of dimensions 1 × 1 mm square (Fig. 3). All the particles that landed on each cell were counted and grouped into a number of smaller size ranges (or classes). The particle population at each cell was statistically analyzed to find the mean values of the temperature, velocity, and size using the standard statistical formula. The calculations were repeated for every cell in the substrate domain, giving the number averaged particle temperature, velocity, and size for each cell.

Table 3 Physical and Thermal Properties of Yttria Stabilized Zirconia[21]

Property	Value
ρ, kg/m^3	5890
T_m, °C	2700
T_{bp}, °C	5000
H_{sf}, J/kg	710 000
C_p, J/kgK	(a)
k, W/mK	2.4

(a) $C_p = 1.06343 \times 10^{-6} T^3 - 2.188953 \times 10^{-3} T^2 + 1.709671 T + 1.466367 \times 10^2$ $273 < T < 873$

$C_p = 678.5$ $T > 873$

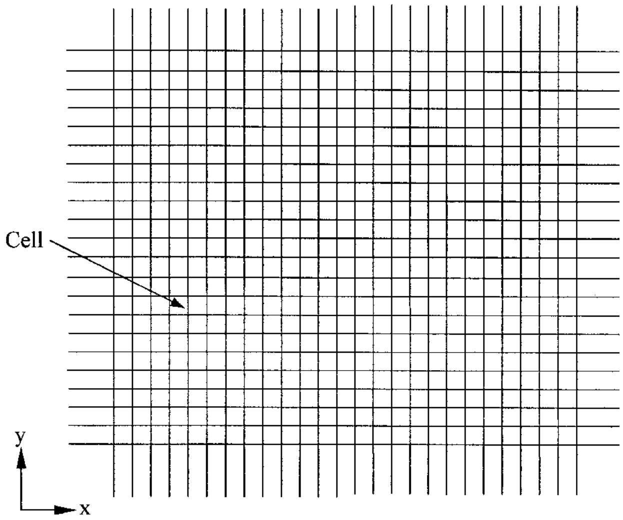

Fig. 3 Division of substrate domain into cells with cell sizes 1 × 1 mm for contour plots and 8 × 8 μm for deposition thickness calculation

2.2.1 Number Averaged Values. The number averaged mean value of particle parameters was calculated by the following equation:

$$\text{Mean } \phi = \frac{\sum_{i=1}^{N} n\,\phi}{\sum_{i=1}^{N} n} \qquad \text{(Eq 12)}$$

where Mean ϕ is the number averaged value of particle in-flight parameters, which can represent temperature, velocity, and size; ϕ is the class mean for the size range under consideration; n is the number of particles in a class; and N is the total number of classes. Figure 4 shows the histogram of all the size ranges and number of all injected particles.

2.2.2 Mass Averaged Values. The number averaging of particle velocity and temperature as defined by Eq 8 neglected the size (therefore their mass and inertial qualities) of the particles. The energy and momentum gained by the particles are dependent on their size and hence the mass. A better physical insight into the energy and momentum acquired by the particle would be gained through the mass averaged velocity and temperature, as it represents the true kinetic and thermal energy acquired by the particles.

Mass averaged temperature and velocity. Particle mass averaged temperature is defined as the total sensible heat gained by all the injected particles divided by the total heat capacity of the injected particles. Otherwise stated, all particles, irrespective of size, will reach the constant mass averaged temperature with the same amount of heat energy that is presently spread over the whole spectrum of different particle sizes and temperatures. Assuming a constant specific heat capacity for the particle material, the total sensible heat gained by all the particles is

$$\sum_{j=i}^{N}\left(\sum_{i=1}^{n} c_p m_{ij}(T_{ij} - T_o)\right)$$

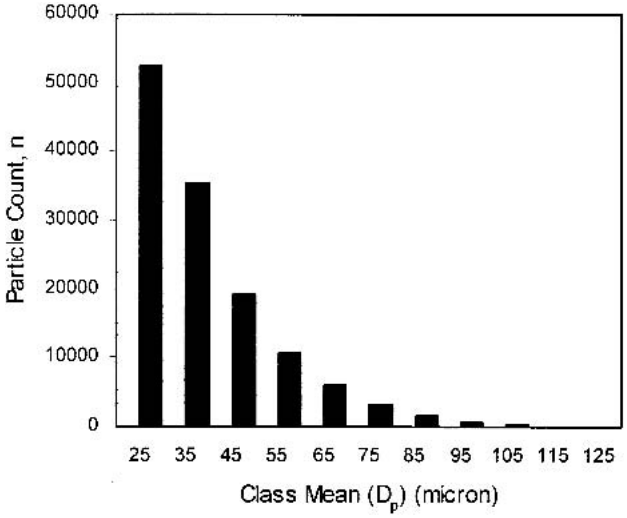

Fig. 4 Particle count distribution of the feedstock, partially stabilized zirconia (YSZ), each class from 10 μm diameter ranges

The specific heat capacity is c_p, m is the mass of particle, $(T - T_o)$ is the temperature gained, n the total number of particles in a class, and N is the total number of classes (detailed in Section 2.2). Hence, the mass averaged particle temperature is

$$T_{\text{mean}} = \frac{\sum_{j=1}^{N}\left(\sum_{i=1}^{n} c_p m_{ij}(T_{ij} - T_o)\right)}{\sum_{j=1}^{N}\sum_{i=1}^{n} c_p m_{ij}} \qquad \text{(Eq 13)}$$

If the sum of momentum of all the particles within the spectrum of sizes (masses) and velocities were to be redistributed in a manner that all the particles have the same velocity, it will be the momentum based mass averaged velocity as defined below. From the momentum of a single particle of (m, V), the mass averaged velocity may be defined as

$$V_{\text{mean}} = \frac{\sum_{j=1}^{N}\left(\sum_{i=1}^{n} m_{ij} V_{ij}\right)}{\sum_{j=1}^{N}\sum_{i=1}^{n} m_{ij}} \qquad \text{(Eq 14)}$$

The notations are as described in the earlier equation. Equations 13 and 14 were evaluated by means of a program that calculated the mass averaged temperature and velocity for the entire lot of injected particles.

2.2.3 Coating Thickness Distribution. The particle impact on the substrate and the splatting of molten particles result in the formation of coating. The spread dynamics are governed by the interplay of parameters such as the inertial, viscous and surface tension forces, substrate geometry, liquid-solid contact between the droplet and substrate, heat transfer between the droplet, and the thermal properties of the substrate.

The splatting model (Pasandideh-Fard[1]) presented here was based on the assumption of fully molten particles that only those particles having a temperature above the melting point was included in calculating thickness distribution. However, it could be assumed that the amount of semi-molten particles, which would stick to the substrate, will be relatively negligible compared to the fully molten and unmelted particles. The successive deposition and splat formation of the molten particles on the substrate resulted in the coating formation by layer-by-layer thickness accumulation.

In the present analysis, it is assumed that the fully molten particles of diameter D_p upon impacting onto the substrate spread into a circular disk shape of diameter d. The maximum spread factor

$$\xi_{\max} = \frac{d}{D_p}$$

was calculated as a function of Weber number,

$$W_e = \frac{\rho_p U_p^2 D_p}{\sigma}$$

Reynolds number,

$$R_e = \frac{\rho_p U_p D_p}{\mu_p}$$

Stefan number,

$$S_t = \frac{C_p(T_p - T_s)}{H_{sf}}$$

and Peclet number,

$$P_e = \frac{V_p D_p}{\alpha}$$

$$\xi_{\max} = \sqrt{\frac{We + 12}{4\dfrac{We}{\sqrt{Re}} + We\sqrt{(3St/4Pe)}}} \qquad \text{(Eq 15)}$$

and the thickness of the splat h is given by

$$h = \frac{2D_p^3}{3d^2} \qquad \text{(Eq 16)}$$

For the spread calculations a grid, shown in Fig. 3, was used with a cell size of 8 × 8 μm. For sufficient roundness of the splat, the size of the cell has to be much less than the smallest diameter splat. This is judged by ensuring that the difference between the circular area of the splat disc and the total approximated accumulated cell area is less than 2% of the latter area.

3. Results and Discussion

In the following sections, the state of the particle, namely temperature, velocity, size, and deposition thickness on the substrate, will be discussed. The cause and effect of process parameters on the distribution of particles on the substrate are of interest.

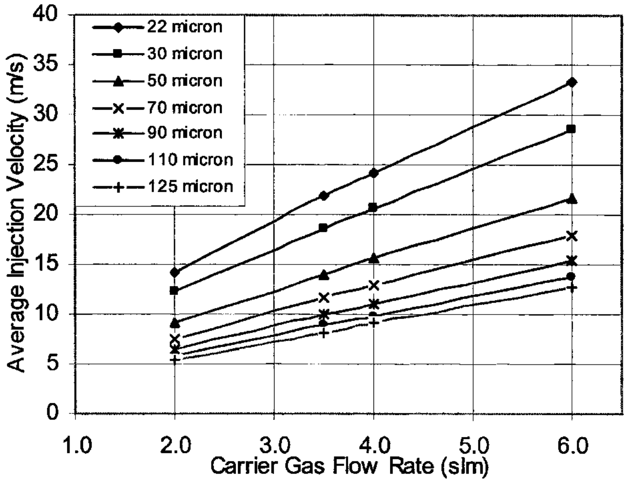

Fig. 5 Computed injection velocity of a range of particle diameters for various carrier gas flow rates at the inboard end of the powder injection port

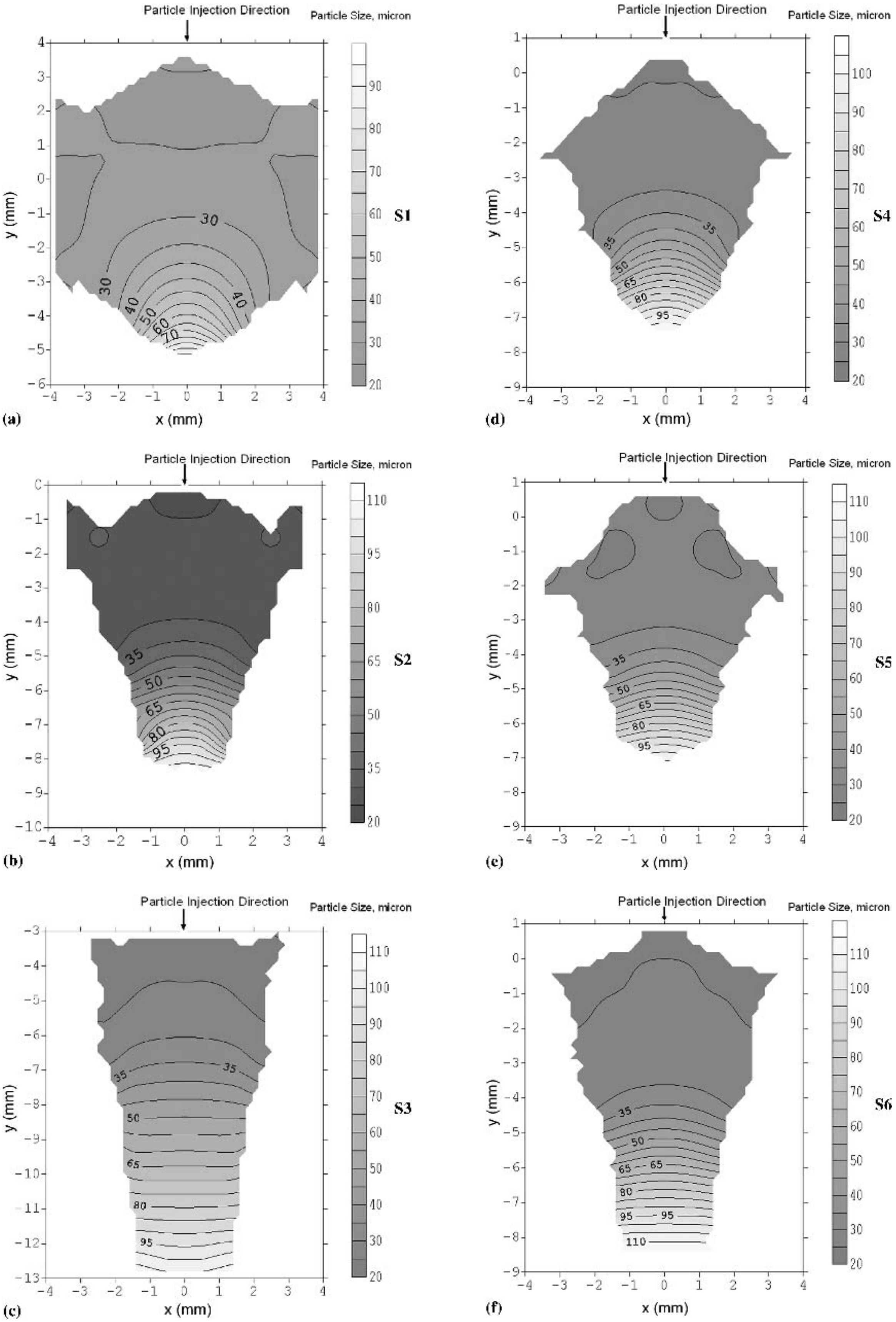

Fig. 6 Contour plots of computed particle diameters at the substrate for cases S1 to S6

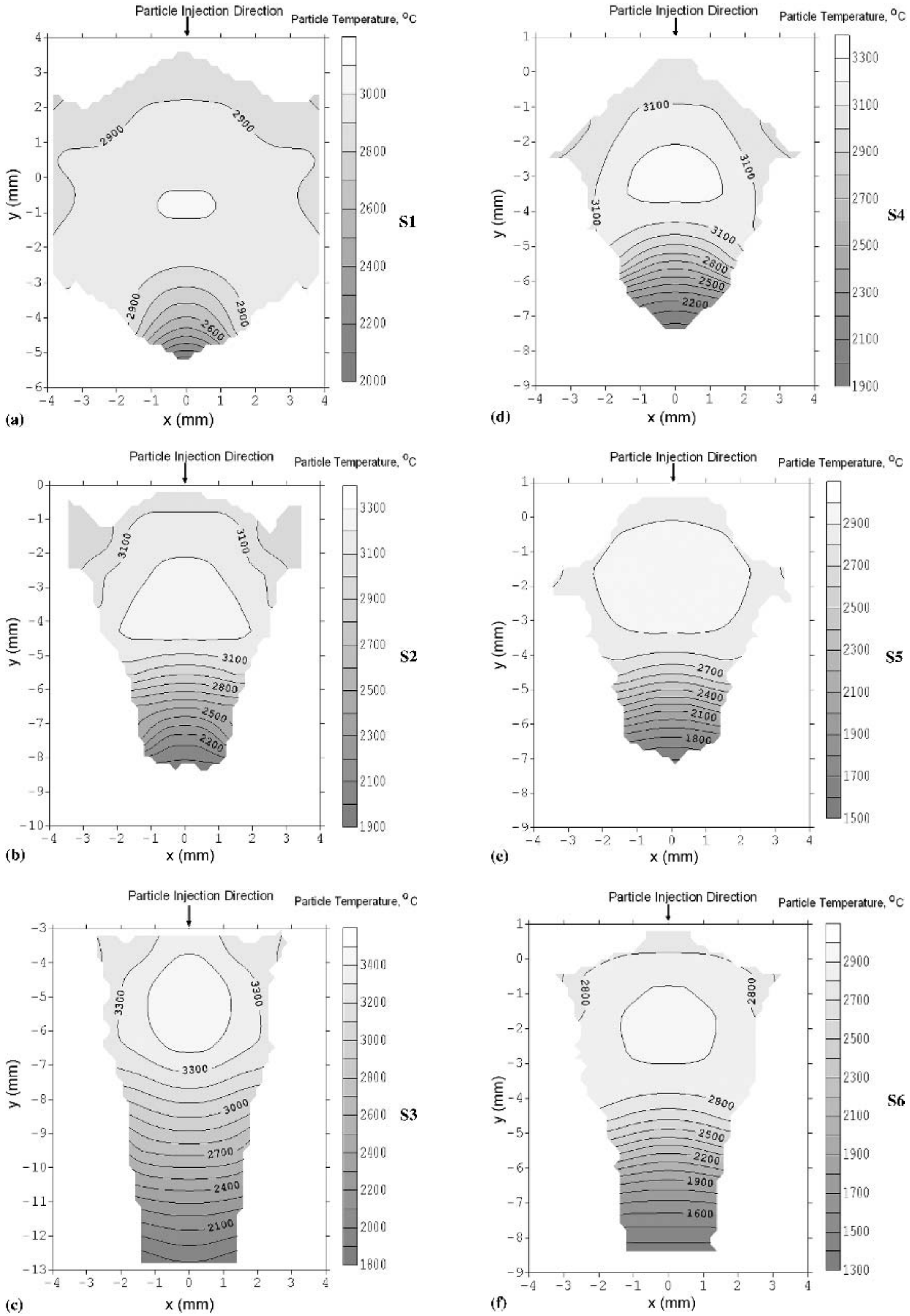

Fig. 7 Contour plots of particle temperature at the substrate for cases S1 to S6

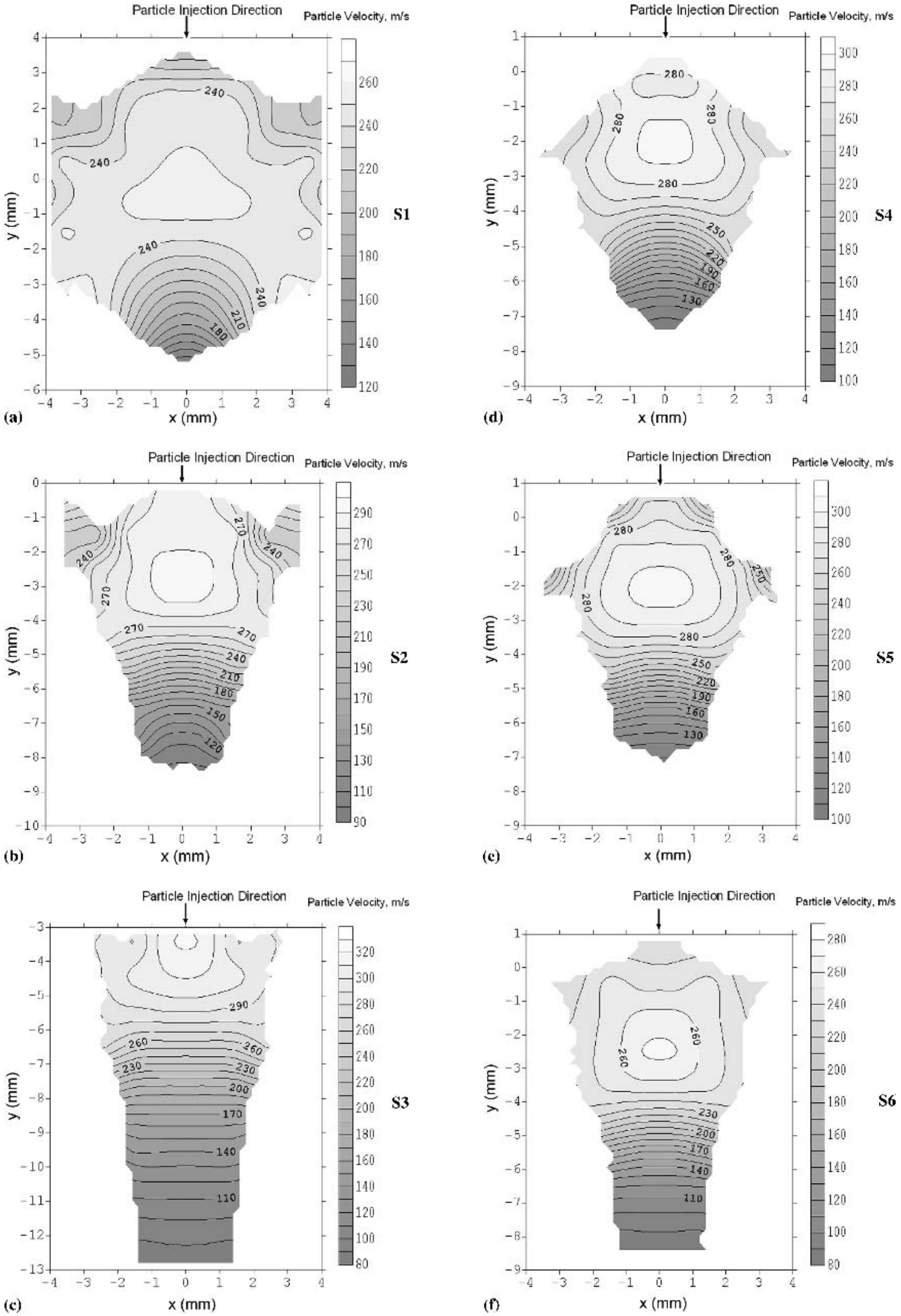

Fig. 8 Contour plots of particle axial velocity at the substrate for cases S1 to S6

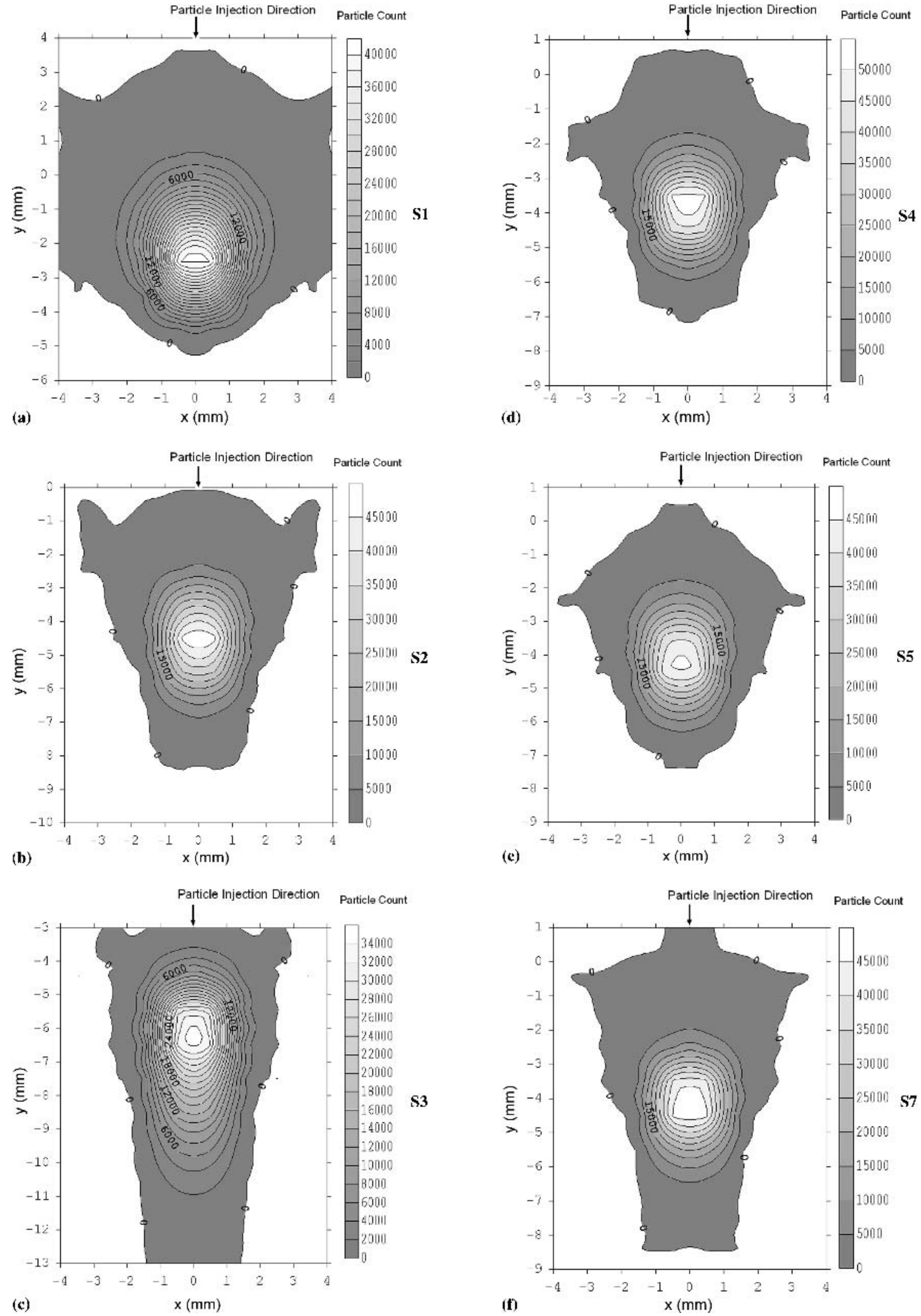

Fig. 9 Particle count (irrespective of size) distribution at the substrate for cases S1 to S6

3.1 Particle Injection Velocity

The most important factor that affects the particle temperature and velocity inside the plasma plume is its trajectory. This depends on whether the particle trajectory mainly resides within the plasma core or outside it. The particle injection velocity determines the particle trajectory that in turn is dependent on the carrier gas flow rate. Particle injection velocity is the particle exit velocity from the inboard end of the particle injection port just before it enters the plasma plume.

Figure 5 shows the variation of average particle injection velocity against the carrier gas flow rate for various particle sizes. It is noted that injection velocity varies linearly with the carrier gas flow rate for a particle of fixed size. The injection velocity also decreases with increasing particle size. Despite their lower velocity, larger particles possess greater momentum enabling them to penetrate plasma jet. Although larger particles are subjected to a relatively greater drag force, due to higher inertia, they will accelerate slower than smaller particles. Thus, smaller particles have higher overall in-flight velocities than larger particles.

3.2 Particle Parameters at Various Positions in the Plume Cross Section

Computation of particle mean temperature and velocity were carried out case-by-case based upon the process parameters shown in Table 2. The temperature, velocity, particle size, and particle number count contours were plotted for cases S1 through S6. The *x-y* plots (Fig. 6-9) with torch axis as the origin (0,0) of the plots with data cells as shown in Fig. 3. The plane shown in contour plots is the plane perpendicular to the torch axis at the standoff distance as shown in Fig. 1. The contour plots of mean particle size, temperature, and velocity on reaching the substrate have been plotted in Fig. 6, 7, and 8 respectively. Also, the contour plot of particle count irrespective of its size at the substrate is plotted in Fig. 9.

3.2.1 Particle Size Distribution at Substrate. From the plot of injection velocity in Fig. 5, it was seen that smaller particles attain higher injection velocity and vice versa. Although the velocities are higher for smaller particles, larger particles penetrate further into the plasma jet compared with the smaller particles due to the higher momentum, as is evident from the particle size contour plot shown in Fig. 6. It can be observed that as the carrier gas flow rate increases, there is a tendency of smoothing out the particle distribution (S1 → S4 → S2 → S3 in increasing order), with an even distribution for the highest carrier gas flow rate (S3). This is due to the high carrier gas flow rate, which increases particle spread (detailed in Section 3.5), hence resulting in the even distribution of particles. A similar trend can be observed for low power level (S6). This is due to the fact that as the arc power is decreased, plasma velocity decreases. When the carrier gas flow rate remains the same, lower plasma velocity results in increased spreading of the deposit profile.

3.2.2 Particle Temperature Distribution at Substrate. The temperature of the larger sized particles tends to be lower, and they tend to congregate at the lower half of the centerline as shown in Fig. 7. Conversely, smaller particles tend to impact near the upper half of the substrate and also with higher temperatures. This could be understood by comparing the particle size distribution at the substrate in Fig. 6 along with particle temperature distribution in Fig. 7. From the particle size distribution, it is seen that smaller sized particles populate the upper half of the substrate and larger sized particles populate the lower half of the substrate. This is due to the fact that the larger sized particles with their higher momentum penetrate well inside the plasma jet and get deposited on the lower half of the plume.

The distribution is more even as the carrier gas flow rate is increased (cases S1 → S4 → S2 → S3 in increasing order). This implies that the increase of carrier gas flow rate results in a wider spread of particles inside the plasma plume along the injection direction.

The heat absorbed by a particle is volume multiplied by specific heat. Thus a particle requires eight times (d^3) the heat for attaining the same temperature rise as compared with another particle with half the diameter of larger particle. At the same time, the surface area of the larger particle through which the heat transfers increased by four times (d^2) compared with a particle with half the diameter. Hence, the heat absorbed per unit volume is the inverse of the particle diameter ($1/d$). When surrounded by the same plasma temperature field, the smaller particle will attain a higher temperature the larger particle, because the smaller particle has a larger heat absorbed per unit volume.

3.2.3 Particle Velocity Distribution at Substrate. A trend similar to the temperature distribution can also be seen in the velocity distribution shown in Fig. 8. The particle velocities are higher at the top of the particle plume and lower at the bottom. From the contour plot of particle size in Fig. 6, it can be observed that the particles have been segregated into bands with smaller sized particles banding near the centerline and larger particles near the bottom. This is expected as the higher sized particles having higher injection momentum will penetrate well into the plasma plume and deposit near the bottom of the centerline.

In the plasma jet, a particle is propelled by the drag force acting on its surface. Due to drag force being proportional to surface area (d^2), a larger particle will be accelerated by a force approximately four times greater than a smaller particle with half the diameter of the larger particle under the same velocity field. From a particle dynamics viewpoint, smaller particles can accelerate or decelerate much faster than larger particles because the larger particle is propelled by four times (d^2) more force, but it now has eight times (d^3) more inertia that needs to be accelerated. Therefore, due to the higher mass, larger sized particles will accelerate or decelerate much slower compared with the smaller sized particles under the same flow field.

3.2.4 Particle Count Distribution at Substrate. In the particle count distribution or particle concentration in Fig. 9, it is observed that the particle plume centerline shifts downward as the carrier gas flow rate is increased. The particle plume centerline is the locus of the points with maximum particle flow in the particle plume. It is observed that the centerline is deviated below the torch centerline by 2.5, 4.2, 4.5, and 6 mm in the *y* axis for carrier gas flow rates of 2, 3.5, 4, and 6 slm (cases S1, S4, S2, and S3), respectively. This observation shows that in case S1, the centerline has shifted only 2.5 mm below the torch axis on reaching the substrate. Therefore, the particle flight was confined in the upper part of the plasma jet core where the plasma temperature is low. In case S3, the centerline has shifted by 6

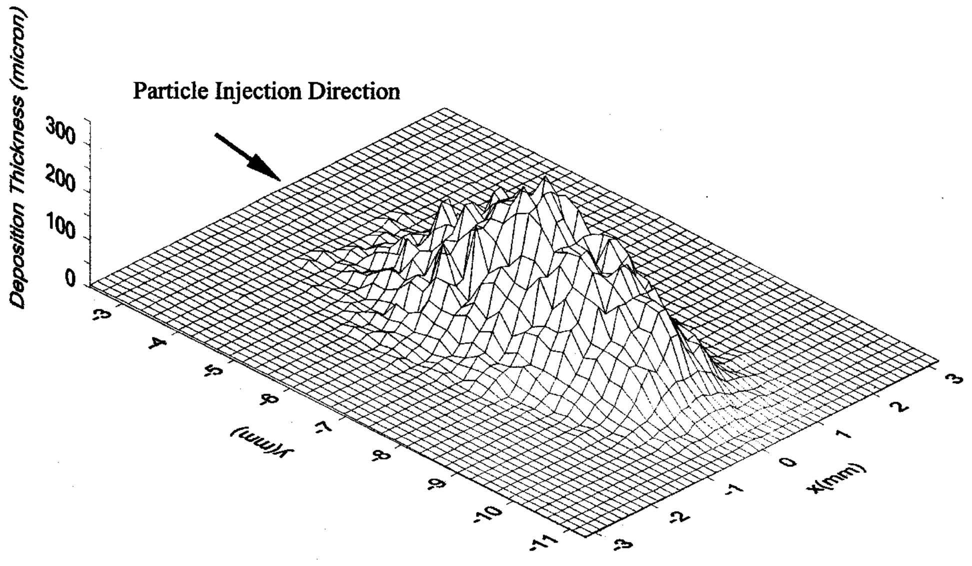

Fig. 10 Snapshot 3D plot of deposit profile at the substrate for case S3 for an exposure time of 1 s

mm below the torch axis showing that it overpenetrated the plasma plume and resulted in the lower particle temperature again. However, in cases S2 and S4 the centerline shifted by approximately 4 mm, showing the particle in-flight was better confined within the jet core, resulting in higher velocity and temperature of the particles.

3.3 Particle Deposition Profiles

The 3D plot of coating profile for a stationary torch for case S3 is as shown in Fig.10. This shows that there is an elongation for the deposition profiles in a direction parallel to the particle injection compared with the lateral direction. The coating thickness profile gives an indication of surface deposit at the substrate in terms of maximum thickness and width of spread. In thermal spray process, the deposition thickness formed account for the particles that have melted and have physically adhered to the substrate. The true deposition thickness will be lower than that predicted in the calculation due to particle evaporation, bouncing of partially melted particles from the substrate and other losses which were not accounted in the simulation. However, the 3D view is sufficiently realistic when compared with experimentally obtained profiles.

Figure 11(a) and (b) shows the simulated deposit sections obtained when the torch is traversed at a speed of 30 cm/s and particle feed rate of 2 g/min. The traverse direction is along the *x* axis of Fig. 10, which results in a stripe of deposit in the *x* direction. The section plotted in Fig. 11(a) and (b) is cut in the *y-z* plane. Wider particle spreading over the substrate with increased carrier gas flow rate is noted in the case S3. This was observed in the experimental spraying done by Kucuk et al.[19] Figure 11(a) shows that the carrier gas flow rate alters the deposition thickness by influencing the dispersion of particles and by the degree of particle melt. Cases S1 and S3 have a lower deposition thickness in comparison to cases S2 and S4; this is due to two reasons. First, in case S1, the amount of melted particles was less, as can be seen in Fig. 11(a), due to the nonoptimized carrier gas flow rate and hence trajectory. Secondly, in case S3, it is due to the larger particle dispersion rendered by a higher rate of carrier gas flow.

In Fig. 11(b), it can be seen that the increase in the primary to secondary gas volume fraction of 3.3 in case S4— to 4.54 in case S5— resulted in lowering in deposition thickness. Subsequently, the decrease in power from S5 to S6 further decreased deposition thickness. The increase in primary gas flow rate in case S5 resulted in lower plasma flame temperatures and hence the heat transferred to the particles. The decrease in power in case S6 resulted in lowering of particle temperature and hence the amount of melted particles. It can be observed that the peak deposition thickness occurred at the same radial distance (approximately 5 mm away from the torch axis) for cases S5 and S6.

3.4 Melted Particle Fraction

The melted particle fraction is defined as the percentage by mass of all particles that attained temperatures above the melting point to the total mass of injected particles. This fraction gives an indication of the quantity of particles that has attained the melting point that will adhere and splat on impact to the substrate. However, care should be taken in analyzing this data, as a higher value of melt fraction does not necessarily indicate better deposition efficiency. For smaller-sized particles, the temperature may be well above the melting point, and this would lead to the evaporation of the particles and hence lower the mass deposition.

For the purpose of comparison, an increase in carrier gas as seen in Fig. 12(a) resulted in a higher melt fraction indicating that more heat was acquired by the particles for cases S1 to S4. In cases S4 and S5, as seen in Fig. 12(b), an increase in total arc gas flow rate as well as primary to secondary gas ratio reduced the melt fraction to a low value. This indicates that increases in total arc gas flow rate resulted in lowering the enthalpy density of plasma gas and hence low melt fraction. Comparing cases S5

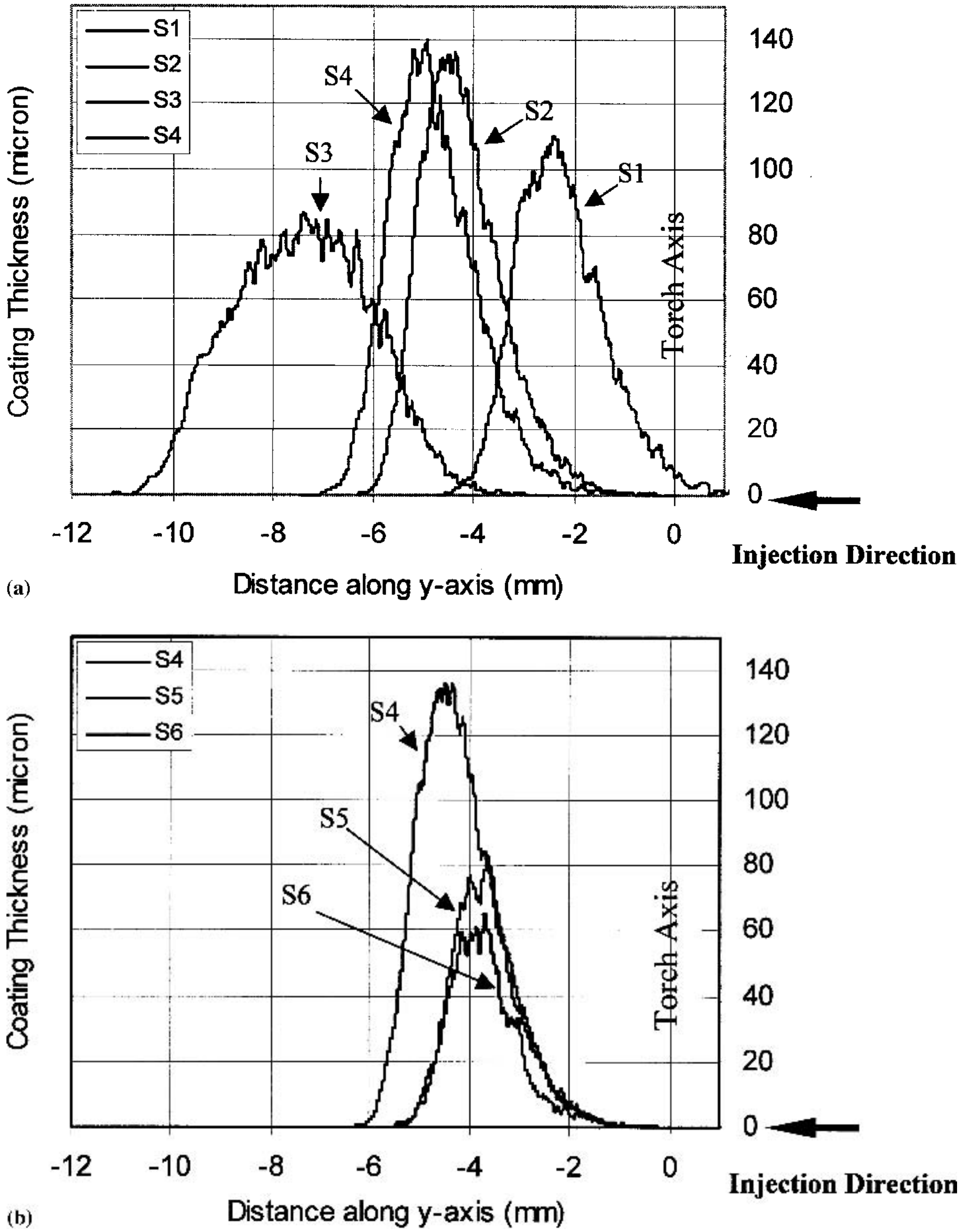

Fig. 11 Particle deposition profile along the symmetric y axis ($x = 0$) for cases S1 to S6

and S6, it can be seen that lowering torch power input from 42 to 33 kW resulted in lowering the melt fraction. The low power input resulted in low enthalpy density of the plasma and hence lowering the melt fraction.

3.5 Particle Residence Time

Particle residence time is defined as the time of flight by the particles from the exit of the particle injection port to impact on the substrate. The longer residence time will increase the heat transferred to the particles. Considering cases S1 to S4 in Fig. 13, it is noted that the particle residence time generally increases with particle size for all cases since the larger particles have lower velocity. Additionally, the increase of carrier gas flow rate generally shortened the residence time.

3.6 Differences Between Number and Mass Averaged Quantities for Temperature and Velocity

In Sections 2.2.1 and 2.2.2, the calculations for number and mass averaged values for temperature and velocity were performed. The mass average is a new quantitative measure that takes into account the mass of the particle. This is a better physical basis since the particle mass has a significant impact on temperature and velocity as shown in this work. In a population of particles with both widely varying sizes and count for each size, the mass average would give a better indication of the overall behavior of the population than the number average. In the limit, if all the particles were of the same size, the two averages would be equal.

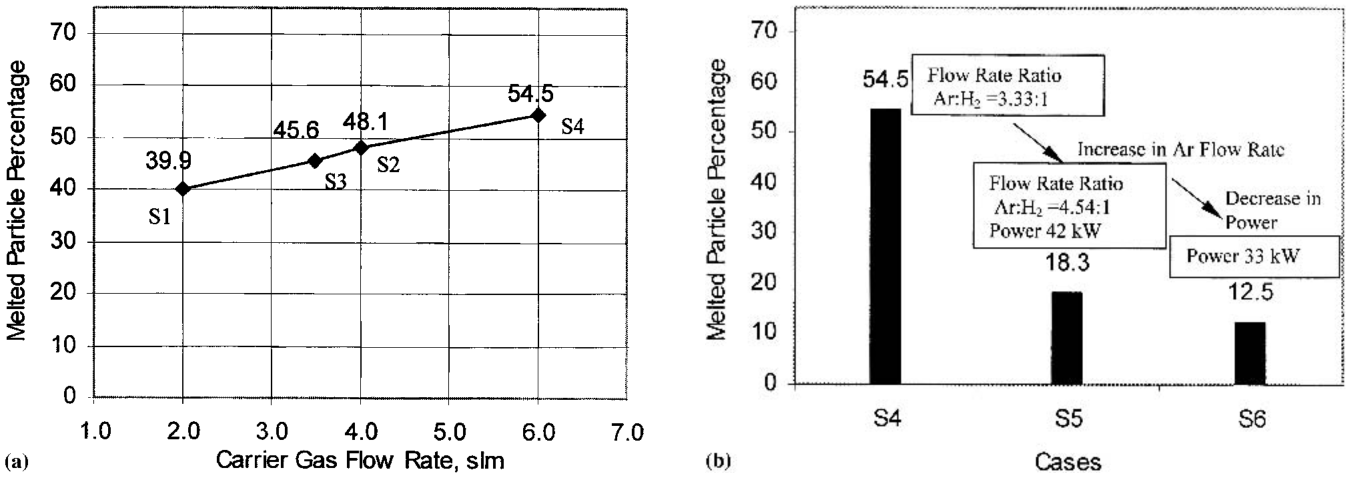

Fig. 12 Mass percentage of particles attained temperature above melting point for **(a)** cases S1 to S4 in which carrier gas flow rate was increasing **(b)** cases S4 to S6 in which carrier gas flow rate was held constant

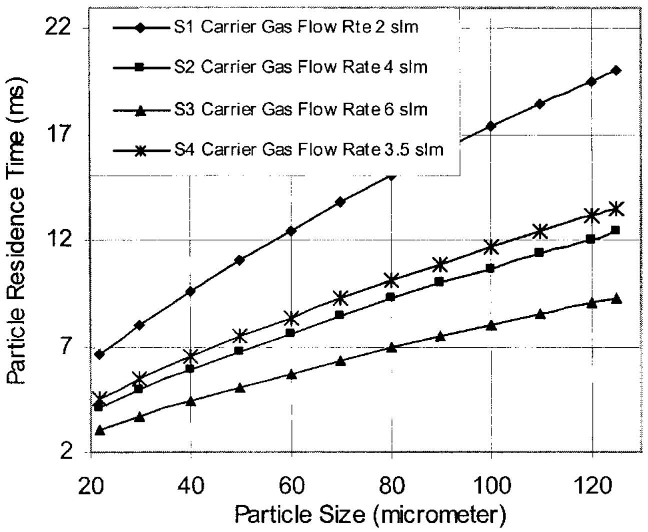

Fig. 13 Particle residence time before it reaches the substrate as carrier gas flow rate increases

It is therefore interesting to compare the two averages for temperature (Fig. 14a,b) and velocity (Fig. 15 a,b), calculated accordingly. For temperature, the number average is consistently between 14 and 18% higher than mass average in all cases. When considering the melting point of zirconia at 2700 °C, the number averaged temperature for cases S1 to S4 are above the melting point. However, the mass averaged temperatures are below the melting point for cases S1, S4, and S2. For the velocity comparisons, the number average values were also higher. Since the velocities do not have a critical value, it can be said that the number average is, in fact, higher by approximately 35-46% in all cases.

The above referenced phenomena of higher recorded values for number average compared with mass average is due to the faster heating and acceleration of smaller particles compared with larger particles. Additionally, in the particle size distribution, smaller particles were higher in number compared with larger particles. From the above, it could be concluded that the mass averaging would provide a better basis for comparison for process efficiency in terms of particle velocity and temperature.

4. Conclusions

The paper presented two major aspects: a study of the distribution of particle in-flight properties and deposition profiles on the substrate for various operating conditions. The plotted results were able to establish some trend relationships between operating parameters and particle behavior.

It is found that carrier gas flow rate influences the particle temperature and velocity as well as the coating distribution on the substrate. Increase in carrier gas resulted in increased dispersion of the particles, but reduced deposition thickness. Carrier gas flow rate altered the particle trajectory by changing the injection velocity, and this resulted in the varied behavior of particles inside the plasma jet. The particle size segregation as reported by experiments[4] was confirmed in this study. Therefore, nonuniformity in the coating quality would result from single-port injection mode. The plotting of the 3D thickness profile yielded a means to compare with the experimentally obtained coating, thus allowing for improvement on the process parameter and operating conditions. Experiments are currently being conducted to correlate actual coating profiles against numerical results. Results of these comparisons will be presented in the future.

The new measurands, i.e., the mass averaged particle temperature and velocity, provide a physically sound basis for process condition monitoring.

Acknowledgment

The first author (K.R.) takes this opportunity to thank Nanyang Technological University (NTU), Singapore for providing financial support for carrying out this research work through the research fund AcRF: 26/96.

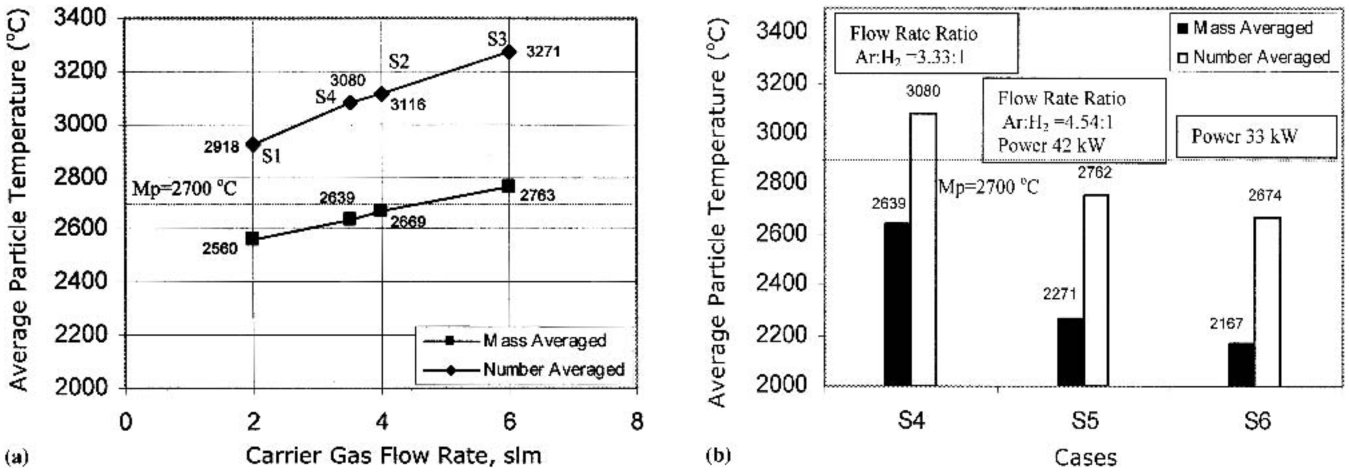

Fig. 14 Influence of **(a)** carrier gas flow rate and **(b)** other process parameters on global number averaged and mass averaged particle temperature

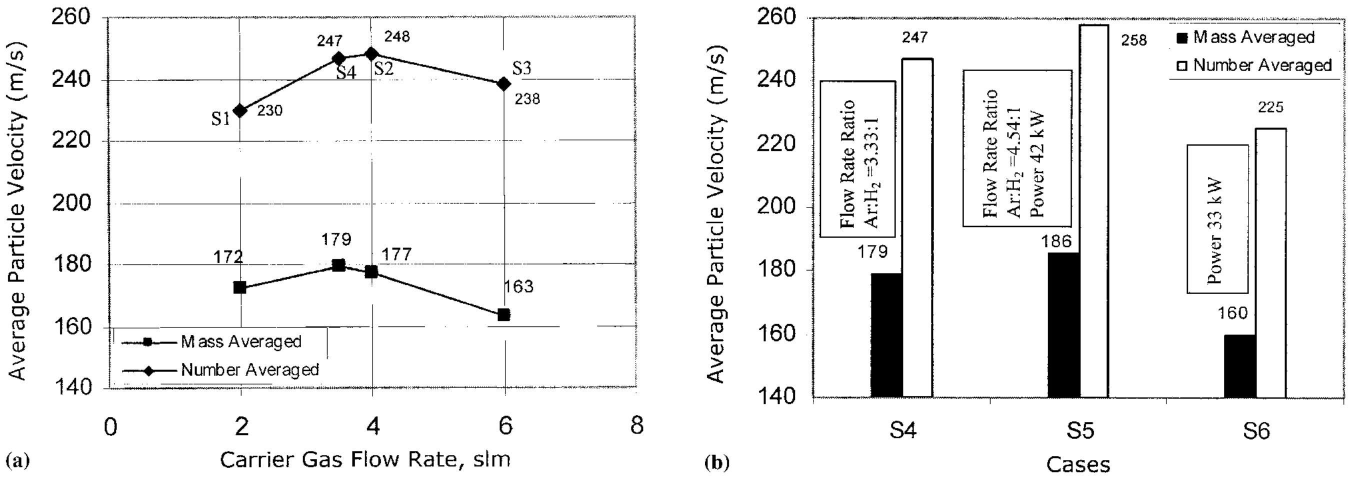

Fig. 15 Influence of **(a)** carrier gas flow rate and **(b)** other process parameters on global number averaged and mass averaged particle velocity

References

1. M. Pasandideh-Fard, R. Bhola, S. Chandra, and J. Mostaghimi: "Deposition of Tin Droplets on a Steel Plate: Simulations and Experiments," *Int. J. Heat Mass Transfer,* 1998, *41,* pp. 2929-45.
2. A. Vaidya, G. Bancke, S. Sampath, and H. Herman: "Influence of Process Variables on the Plasma Sprayed Coatings: An Integrated Study" in *Thermal Spray 2001: New Surfaces for New Millennium,* C.C. Berndt, ed., ASM International, Singapore, 2001, pp. 1345-49.
3. L. Pawlowski: *The Science and Engineering of Thermal Spray Coatings*, John Wiley & Sons, West Sussex, England, 1995.
4. B.M. Cetegen and W. Yu: "In-Situ Particle Temperature, Velocity, and Size Measurement in DC Arc Plasma Thermal Sprays," *J. Thermal Spray Technol.,* 1999, *8*(1), pp. 57-67.
5. M. Vardelle, A. Vardelle, and P. Fauchais: "Spray Parameters and Particle Behaviour Relationships During Plasma Spraying," *J. Thermal Spray Technol.,* 1993, *2*(1), pp. 79-91.
6. M.I. Boulos, P. Fauchais, A. Vardelle, E. Pfender.: "Fundamentals of Plasma Particle Momentum and Heat Transfer" in *Plasma Spraying: Theory and Applications*, R. Suryanarayanan, ed., World Scientific, Singapore, 1993, pp. 3-57.
7. J.R. Fincke, W.D. Swank, and C.L. Jeffery: "Simultaneous Measurement of Particle Size, Velocity and Temperature in Thermal Plasmas," *IEEE Trans. Plasma Sci.,* 1990, *18*(6), pp. 948-57.
8. W.D. Swank, J.R. Fincke, and D.C. Heggard, "Behaviour of Ni-Al Particles in Argon:Helium Plasma Jets," *J. Therm. Spray Technol.,* 1993, *2*(3), pp. 243-49.
9. J.R. Fincke, W.D. Swank, C.L. Jeffery, C.A. Mancuso: "Simultaneous Measurement of Particle Size, Velocity and Temperature," *Meas. Sci. Technol.,* 1993, *4,* pp. 559-65.
10. M. Jian, S.C.M. Yu, H.W. Ng, and Y.C. Lam: "Measurement of Size and Velocity Characteristics in Plasma Spraying Process Using PDA, Paper AIAA: 2001-2930" in *32nd AIAA Plasma Dynamics and Lasers Conference*, Anaheim, CA, 2001.
11. A. Kucuk, R.S. Lima, and C.C. Berndt: "Influence of Plasma Spray Parameters on In-Flight Characteristics of ZrO2-8 wt % Y2O3 Ceramic Particles," J. *Am. Ceram. Soc.,* 2001. *84*(4), p. 685-92.
12. K. Remesh, S.C.M. Yu, and H.W. Ng: "Computational Study and Experimental Comparison of the In-flight Particle Behavior for an External Injection Plasma Spray Process," *J. Thermal Spray Technol.* (in press).
13. J. Madejski: "Solidification of Droplets on Cold Surface," *Int. J. Heat Mass Transfer,* 1976, *19,* pp. 9-20.
14. R. McPherson: "The Relationship Between the Mechanism of Formation, Microstructure and Properties of Plasma Sprayed Coatings," *Thin Solid Films,* 1981, *83,* pp. 297-310.
15. R. Ghafouri-Azar, J. Mostaghimi, and S. Chandra: "Deposition Model of Thermal Spray Coating" in *International Thermal Spray Conference*

and Exhibtion, C.C. Berndt, ed., ASM International, Materials Park, OH, 2001.

16. H. Zhang, "Theoretical Analysis of Spreading and Solidification of Molten Droplet During Thermal Spray Deposition," *Int. J. Heat Mass Transfer,* 1999. *42,* pp. 2499-2508.
17. M. Fukumoto and Y. Huang: "Flattening Mechanism in Thermal Sprayed Nickel Particle Impinging on Flat Substrate Surface," *J. Thermal Spray Technol.,* 1999, *8*(3), pp. 427-32.
18. M. Fukumoto, E. Nishioka, and T. Nishiyama: "Proposal of New Criterion for Splashing of Thermal Sprayed Particle Onto Flat Substrate Surface" in *Thermal Spray 2001: New Surfaces for a New Millennium*, C.C. Berndt, ed., ASM International, Materials Park, OH, 2001, pp. 841-48.
19. A. Kucuk, R.S. Lima, and C.C. Berndt, "Influence of Plasma Spray Parameters on Formation and Morphology of ZrO2 - 8 wt% Y2O3 Deposits," *J. Am. Ceram. Soc.,* 2001. *84*(4), p. 693-700.
20. M.I. Boulos, P. Fauchais, and E. Pfender, *ThermalPlasmas: Fundamentals and Application*, Vol. 1, Plenum Press, New York, NY, 1994.
21. Anon: *The CRC Material Science and Engineering Hand Book*, J.F. Shackelford and W. Alexander, ed., CRC Press, Boca Raton, FL, 1994.